CHEMISTRY OF MATERIALS

pubs.acs.org/cm

Article

Oxide Ion and Proton Conductivity in Highly Oxygen-Deficient Cubic Perovskite $SrSc_{0.3}Zn_{0.2}Ga_{0.5}O_{2.4}$

Chloe A. Fuller, Quentin Berrod, Bernhard Frick, Mark R. Johnson, Maxim Avdeev, John S. O. Evans, and Ivana Radosavljevic Evans*

Cite This: *Chem. Mater.* 2020, 32, 4347−4357

Read Online

ACCESS | Metrics & More | Article Recommendations | Supporting Information

ABSTRACT: A series of Zn-substituted compounds, $Sr_2Sc_{1-x}Zn_xGaO_{5-0.5x}$, based on the brownmillerite-type oxide ion conductor Sr_2ScGaO_5 have been synthesized, and a single-phase region has been identified at $0.4 \leq x < 0.6$. The structure and dynamics of $Sr_2Sc_{0.6}Zn_{0.4}GaO_{4.8}$ were investigated by X-ray and neutron diffraction, neutron total scattering and pair distribution function (PDF) analysis, impedance spectroscopy, and neutron spectroscopy. The material was found to be a highly disordered cubic perovskite with a remarkable level of oxygen deficiency across a large temperature range. These structural properties lead to an increase of oxide ion conductivity of about two orders of magnitude relative to the parent Sr_2ScGaO_5. The presence of proton conductivity and some water uptake was suggested by the impedance data and corroborated by thermogravimetric analysis (TGA), solid state nuclear magnetic resonance (NMR), variable temperature X-ray diffraction, and neutron spectroscopy. Both proton and oxide ion conductivity produced a measurable quasi-elastic neutron scattering (QENS) signal, and the onset of each dynamic process could be observed by monitoring the temperature dependence of the elastic and inelastic scattering intensities measured in fixed window scans. Neutron total scattering and PDF studies revealed a local structure that is markedly different from the perovskite average structure, and we propose that $Sr_2Sc_{0.6}Zn_{0.4}GaO_{4.8}$ contains a rare one-coordinate or terminal oxygen site.

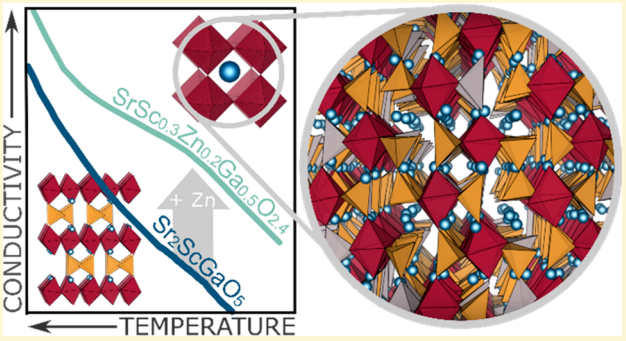

1. INTRODUCTION

The perovskite structure, often adopted by mixed metal oxides of the general formula ABO_3, is one of the most ubiquitous in solid-state chemistry because of the vast number of combinations of the A and B cations it can support. As a consequence of this chemical versatility, perovskite-type oxides display a number of technologically important physical properties: ferroelectricity, piezoelectricity, colossal magnetoresistance, catalytic activity, fast ion conductivity, mixed ionic electronic conductivity, and others. Oxide ion conductivity in perovskites is readily induced by aliovalent (acceptor) doping, generating oxygen-deficient materials. At relatively low doping levels, the cubic perovskite structure can be retained, the vacancies are distributed randomly, and three-dimensional oxide ion diffusion proceeds via a vacancy-hopping mechanism.[1−3]

At higher defect concentrations, ordered structures such as the brownmillerite structure can be formed. With general formula $A_2B_2O_5$, this can be viewed as oxygen-deficient perovskite with one-sixth of the oxygen sites vacant. The oxide ion vacancies are ordered along one crystallographic direction, resulting in alternating corner-sharing octahedral and tetrahedral layers formed by $BO_{6/2}$ and $BO_{4/2}$ groups, respectively. This structural arrangement means that the oxide ion conductivities of brownmillerites are typically lower than their perovskite counterparts as well as being predominantly one-dimensional. For example, orthorhombic brownmillerite-type Sr_2ScGaO_5 is a modest oxide ion conductor ($\sim 10^{-6}$ S cm^{-1} at 600 °C), whereas the conductivity of this material in the high-temperature cubic form is 2 orders of magnitude higher.[4,5] We have recently demonstrated that introducing a small amount of additional (extrinsic) vacancies into the octahedral layer of Sr_2ScGaO_5 by Zn-doping increases the oxide ion conductivity relative to the parent material by up to 2 orders of magnitude, while retaining the orthorhombic brownmillerite structure. We attributed this increase in conductivity and the lowering of the activation energy to the extrinsic vacancies disordered in the octahedral layers,

Received: March 31, 2020
Revised: April 26, 2020
Published: April 27, 2020

providing additional oxide ion migration pathways in the structure.[5]

An alternative way to introduce disorder into perovskite derivatives is to change the ratio of numbers of octahedral and tetrahedral building blocks in the structure. For example, Chernov et al.[6] have described how increasing the GaO_4 tetrahedra to ScO_6 octahedra ratio in the Sr/Sc/Ga/O system leads to an evolving family of structures. $Sr_{10}Sc_4Ga_6O_{25}$ ($Sr_2Sc_{0.8}Ga_{1.2}O_5$), for example, is perovskite-related, but the connectivity balance means that coordination polyhedra can no longer share all their corners, and the structure contains a mix of $ScO_{6/2}$, $GaO_{4/2}$, and $GaO_{3/2}O$ units. Tetrahedra that are not fully corner-linked have been shown to facilitate oxide ion mobility in different structural families.[7−10]

In this work, we have used this design approach to prepare new oxide ion conductors of general formula $Sr_2Sc_{1-x}Zn_xGaO_{5-0.5x}$ (x = 0.1−0.6). We show that by increasing the number of tetrahedral sites in a brownmillerite and increasing the oxygen vacancies beyond the 1/6 level, we can re-form highly disordered and highly oxygen-deficient cubic perovskite materials. We report the proton and oxide ion conductivity in this system and the use of variable-temperature powder X-ray and neutron diffraction, neutron total scattering and pair distribution function (PDF) analysis, and inelastic/quasi-elastic neutron scattering to elucidate in detail the structure−property relationships in $SrSc_{0.3}Zn_{0.2}Ga_{0.5}O_{2.4}$.

2. EXPERIMENTAL SECTION

Synthesis. Polycrystalline samples of $Sr_2Sc_{1-x}Zn_xGaO_{5-0.5x}$ (x = 0.1−0.6) were synthesized from stoichiometric amounts of $SrCO_3$ (Fisher Chemical, >99.9%), Sc_2O_3 (Sigma-Aldrich, >99.9%), Ga_2O_3 (Sigma-Aldrich, >99.99%), and ZnO (Alfa Aesar, >99.99%). The starting materials were ground together and heated at 1200 °C for 12 h. Samples were reground, pressed into 10 mm pellets, and heated at the same temperature for a further 24 h. This was repeated until the powder X-ray diffraction (PXRD) patterns no longer changed with additional heating. A Bruker D8 Advance diffractometer equipped with a Lynx-eye detector and Cu Kα radiation was used to monitor the progress of the solid-state reactions. The same instrument was used over an extended 2θ range with a Si internal standard (a = 5.431195(9) Å at room temperature) for accurate cell parameter determination. Analysis of the diffraction data was performed by using the Rietveld method[11] implemented in the Topas Academic software.[12,13] Within this work, specific samples will be referred to by an abbreviated name of the form SSGO (for Sr_2ScGaO_5) or SSZ40GO (for $Sr_2Sc_{0.6}Zn_{0.4}GaO_{4.8}$) where the number in the abbreviation indicates the percentage of Sc that has been replaced with Zn.

Variable-Temperature X-ray Diffraction. VT-XRD patterns of single-phase compositions were recorded on a Bruker D8 Advance (Lynx-eye detector, Cu Kα radiation) with an Anton Paar HTK1200 furnace attachment over a temperature range of 25−1000 °C. Furnace temperatures were calibrated based on an external Al_2O_3 standard.[14] Data were collected every 20 °C on heating and cooling, and resulting patterns were analyzed by Rietveld fitting in Topas Academic.[12,13]

Neutron Powder Diffraction (NPD). Diffraction data were collected on a powdered, 6 g sample of SSZ40GO in a 9 mm vanadium sample can on the high-resolution powder diffractometer ECHIDNA[15] at the OPAL reactor at ANSTO, Sydney. Diffraction patterns were measured using neutrons with a wavelength of 1.6215 Å at room temperature, 200, 300, 400, 500, 700, 800, and 900 °C as well as at −253 °C in a vacuum furnace and cryofurnace.

Chemical Analysis. The elemental composition of SSZ40GO was confirmed by inductively coupled plasma mass spectrometry (ICPMS) analysis using ∼50 mg of powdered sample dissolved in nitric acid with a Thermo Scientific Neptune Plus Higher Resolution Multicollector.

Impedance Spectroscopy. SSZ40GO powder was uniaxially pressed into a 10 mm pellet and sintered for 24 h at 1200 °C, yielding a pellet that was 84% dense. The pellet was coated in platinum ink and mounted on a Probostat A-6 cell. The electrodes were set by heating at 1000 °C for 1 h. A Solartron 1260 frequency-response analyzer was used to measure and record impedance spectra every 20° on heating and cooling in air, dry N_2, and wet N_2 (bubbled through water) using frequency ranges of 0.1−10^7 Hz and voltages of 100−2500 mV.

Thermogravimetric Analysis. A PerkinElmer TGA 8000 instrument was used to measure mass changes on heating and cooling cycles. Multiple samples of SSZ40GO were heated from 30 to 1000 °C and back to ambient temperature at 10 °C min^{-1} under an air atmosphere.

Solid-State NMR. Static ^{45}Sc and ^{71}Ga NMR spectra were recorded at 97.21 and 122.04 MHz, respectively, for both SSZ40GO and SSGO on a Bruker Avance III HD spectrometer using 1 M $Ga(NO_3)_3$ and $ScCl_3$ solutions as references. WURST-qCPMG pulse sequences[16] were used for both experiments yielding spikelet spectra. The ^1H NMR spectrum of SSZ40GO was recorded on a powder sample that had been exposed to air for 2 weeks following synthesis. A Bruker Avance III HD spectrometer with tetramethylsilane as a reference was used for the measurement.

Neutron Total Scattering. Total scattering data on SSZ40GO were collected on the POLARIS instrument at the ISIS facility at Rutherford Appleton Laboratory. A ∼6 g powder sample was packed into an 8 mm diameter vanadium can. Rietveld-quality data sets were collected at 45 temperatures on heating for 4 min each. High-quality data sets for pair distribution function (PDF) analysis were acquired at room temperature, 600 °C, and 1000 °C in eight sets of 175 μAh collections, i.e., 8 h at each temperature. The scattering due to the empty furnace and the empty can were measured at room temperature for 1−2 h each for background subtraction. Neutron total scattering data were normalized onto an absolute scale by using GudrunN software;[17] the $D(r)$ functions used for fitting were extracted using a Q_{max} of 40 $Å^{-1}$ using standard formalisms,[18] and Fourier ripples < r = 1.6 Å were removed. Bragg data were extracted using the established analysis routines in Mantid.[19]

Rietveld and large-box local structure analyses were performed using Topas Academic.[12,13] The three highest resolution data banks (banks 3, 4, and 5) of POLARIS were used for variable-temperature neutron refinements covering a total d-spacing range of 0.15−5.75 Å. Bank 3 was selected for local structure analysis as it offers a good compromise between resolution and Q-range. For PDF fitting, large-box models were constructed by converting appropriate small box models onto a perovskite basis and expanding them to a close-to isotropic supercell containing between 2000 and 8000 atoms. Atomic coordinates were then refined against the data subject to polyhedral constraints to keep local geometry sensible. Bragg and PDF data sets were fitted simultaneously using a fitting range of 2000−20000 μs for Bragg data and 0−19.5 Å for PDF $D(r)$ data. In initial refinement cycles, coordinate changes were constrained to prevent large atomic shifts; these constraints were relaxed during fitting. An equal weighting was applied to each point in the PDF such that the PDF and Bragg data gave a similar contribution to the overall χ^2. PDF patterns were calculated directly from the atomic coordinates of the large box model, and the Bragg scattering was calculated by folding the large-box coordinates back into a single crystallographic unit cell. Refinements converged within a couple of hours on a standard desktop PC. Multiple starting configurations were tested for each model to ensure the final fit could be replicated.

Inelastic and Quasi-Elastic Neutron Scattering. Inelastic neutron scattering data on SSZ40GO were measured on both the backscattering spectrometer IN16B and the time-of-flight spectrometer IN6-SHARP (run by the Laboratoire Léon Brillouin) at the Institut Laue Langevin.

The experiment on IN16B used an incident neutron wavelength of 6.271 Å and an energy resolution of 0.75 μeV to give access to nanosecond dynamics. A 10 g powdered sample of SSZ40GO was placed in a cylindrical 8 mm diameter Nb-foil sample holder, and

https://dx.doi.org/10.1021/acs.chemmater.0c01378
Chem. Mater. 2020, 32, 4347−4357

measurements of elastic intensity (E = 0 μeV) and inelastic intensity at 2 μeV were performed on heating and cooling from 20 to 1000 °C using a heating rate of 0.04 °C s^{-1}. Data points were collected in pairs with an elastic intensity (EFWS: elastic fixed window scan) measured for 30 s, immediately followed by an inelastic intensity (IFWS: inelastic fixed window scan) measurement lasting 2 min.[20] Quasi-elastic neutron scattering (QENS) measurements were performed at room temperature, 300 °C, and 400 °C for 6 h at each temperature (as 12 0.5-h repetitions) and 900 and 1000 °C for 1.5 h each. An energy transfer window of ±20 μeV was used for all QENS data collections. The background scattering from the empty can was measured for 5 h at both room temperature and 400 °C, and a vanadium resolution function was acquired for 4 h at 40 °C. The data were reduced and analyzed by using established routines implemented in the Mantid code.[19]

The IN6-SHARP experiment was performed with an incident neutron wavelength of 5.12 Å and an elastic energy resolution of 70 μeV to give access to picosecond dynamics. Data were collected at 20, 200, 400, 600, 800, and 1000 °C, with a collection time of 6 h at each temperature on the same sample. Background scattering from the empty sample holder was measured for 6 h at 20 °C, and a vanadium standard was measured at 20 °C for 6 h for normalization and to describe the instrument resolution function. Data were processed by using Mantid and LAMP software packages[21] and analyzed using QENSH software.[22]

3. RESULTS AND DISCUSSION

PXRD patterns for each of the samples are shown in Figure S1. They suggest that single-phase compounds with nominal compositions $Sr_2Sc_{1-x}Zn_xGaO_{5-0.5x}$ (x = 0.4 and 0.5) were synthesized successfully. Previous work showed a x = 0.05 sample retained the brownmillerite-type structure adopted by Sr_2ScGaO_5[5] with the same room-temperature space group $I2mb$. Evidence for successful substitution was provided by small changes in the crystallographic a- and b-axes and in the change in conduction behavior.[5] For compositions with 0.4 ≤ x < 0.6, the single-phase product is a cubic perovskite. Increasing the Zn content and B-site disorder therefore appears to lead to the room-temperature stabilization of the high-temperature disordered phase that has been seen in multiple brownmillerites, including $Sr_2Fe_2O_5$ and $Ba_2In_2O_5$.[4,23,24] Compositions with x = 0.1, 0.2, and 0.3 were two-phase, containing the brownmillerite and an increasing proportion of the perovskite. Rietveld refinement shows that the quantities of perovskite and brownmillerite in the 0.05 < x < 0.4 two-phase region are consistent with phase separation into $Sr_2Sc_{0.95}Zn_{0.05}GaO_{4.975}$ (SSZ05GO) and $Sr_2Sc_{0.6}Zn_{0.4}GaO_{4.8}$(SSZ40GO). Finally, the x = 0.6 sample contained mainly the perovskite phase but also a very small amount of an unidentified impurity (top plot in Figure S1).

Since SSZ40GO is a cubic perovskite, we can write its formula as $SrSc_{0.3}Zn_{0.2}Ga_{0.5}O_{2.4}$. Literature examples of perovskites with oxygen contents lower than $ABO_{2.5}$ are uncommon and typically found for compounds containing variable oxidation state transition metals[25−29] (e.g., $Ba_{0.5}Sr_{0.5}Co_{0.8}Fe_{0.2}O_{3-\delta}$ where δ can be up to 1 depending on the p_{O_2}) or in compounds like $SrCuO_2$ and $SrFeO_2$ which have the square-planar-based infinite layer structure.[30−32] These are frequently made by low-temperature topotactic reduction of oxygen-rich phases. On the other hand, Takeda et al.[33] reported oxygen deficiency corresponding to the oxygen content of 2.45 (normalized to perovskite) in the Sr/Ba/Sc/Al/O system. The cubic perovskite materials reported here display even higher oxygen deficiency, corresponding to an oxygen content as low as $ABO_{2.375}$ (SSZ50GO), while containing only fixed-oxidation-state cations.

Average Structure. Powder X-ray and neutron diffraction patterns of SSZ40GO (Figure 1) can be fully fitted using an a = 3.9871 Å perovskite model in the cubic space group Pm-3m. The structural model included Sr on the A-site, Sc, Ga, and Zn on the B site, and O sites in their nominal proportions, confirmed by ICP elemental analysis of the cations. The neutron diffraction pattern shows some structured diffuse scattering that is particularly noticeable at Q = 4.5 $Å^{-1}$. This suggests that there are local deviations from the average structure. The fact that this is seen in the neutron pattern but not the X-ray implies that the deviation occurs mainly on the oxygen sublattice. The local structure of this material is discussed later.

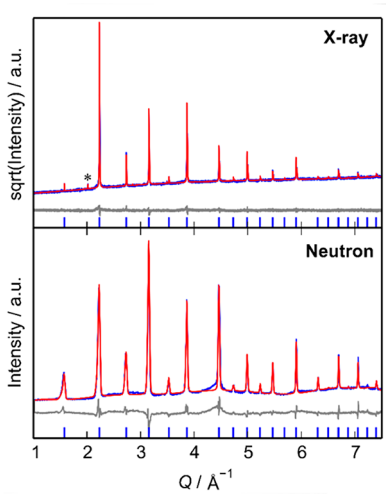

Figure 1. Rietveld fits of a simple Pm-3m perovskite model against the room temperature X-ray (top) and neutron (bottom) data for SSZ40GO. Blue, red, and gray curves show the observed, calculated, and difference curves, respectively. Blue tick marks indicate the expected peak positions. The peak highlighted with an asterisk is as a result of W Lα incident X-ray contamination. X-ray data are shown on a square root scale to emphasize weaker features.

Variable-temperature PXRD was performed across a temperature range of 16−1273 K, and some of the data are displayed in Figure S2. No major change (peak splitting/appearance/disappearance) is observed, indicating that there are no structural phase transitions in this temperature range. The same conclusion can be drawn from the NPD data. X-ray and neutron data show no evidence for brownmillerite-type ordering at low temperature; the fit of the cubic perovskite model to the 20 K NPD pattern is given in Figure S3.

Conductivity. The conductivity of SSZ40GO was measured using impedance spectroscopy between 200 and 1000 °C on both heating and cooling. The complex impedance plots (Figure S4) across the whole temperature range comprised two responses: a large semicircle at high frequency and an electrode response at low frequency. At high temperature the electrode response turned over into a semicircle, indicating diffusion through a finite layer, which suggests conductivity is ionic in nature. The capacitance of the high-frequency semicircle was found to be ∼10^{-12} F cm^{-1} by using the relationship ωRC = 1 at the arc maximum and is consistent with bulk transport.[34] Bulk resistance values were therefore extracted from the high-frequency intercept of the semicircular signal, and the derived

https://dx.doi.org/10.1021/acs.chemmater.0c01378
Chem. Mater. 2020, 32, 4347−4357

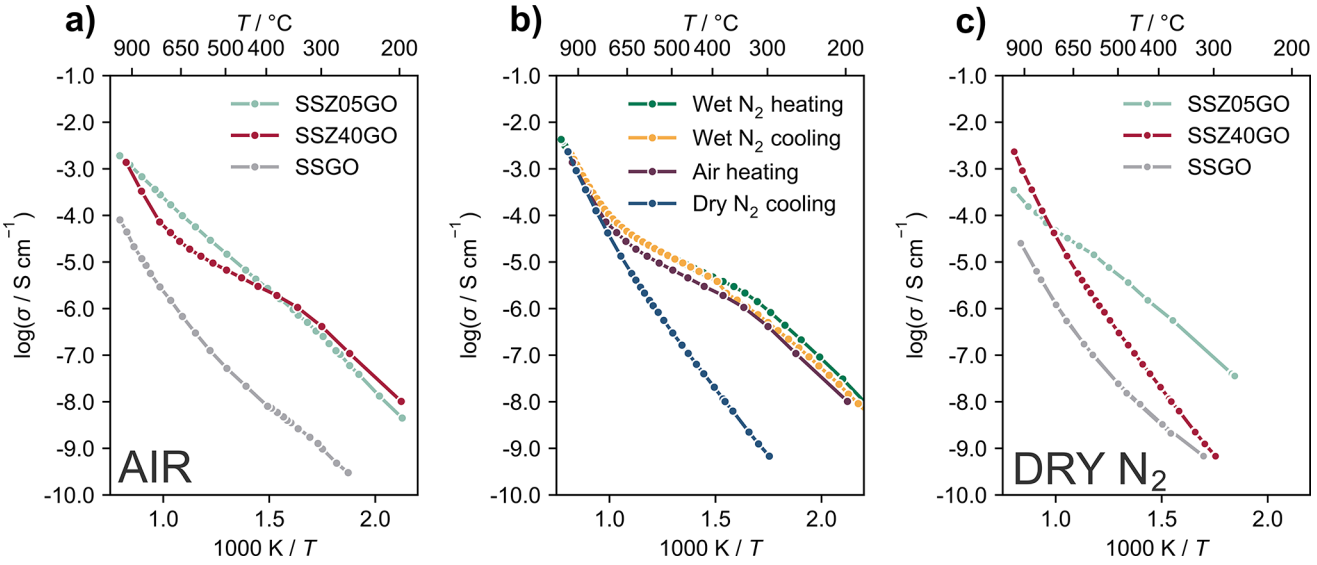

Figure 2. Conductivity as a function of temperature for SSZ40GO and related compounds: (a) comparison of conductivities in air for the different compounds, (b) conductivity under different atmospheres for SSZ40GO, and (c) comparison between conductivities in dry nitrogen for the different compounds. Data shown for SSGO and SSZ05GO are from both heating and cooling cycles.

conductivities are plotted in Figure 2a along with those of the parent material SSGO and related brownmillerite SSZ05GO.[5]

There is an up to 2 orders of magnitude increase in total conductivity in SSZ40GO relative to the parent, and the largest increase occurs at lower temperatures, below 500 °C.

In air, the $\log(\sigma)$ vs $1/T$ plot for SSZ40GO (light green curve in Figure 2a) is nonlinear and can be divided into three broad sections: low temperature (<300 °C), intermediate temperature (300−650 °C), and high temperature (>650 °C). Apparent activation energies for each section were extracted from a plot of $\ln(\sigma T)$ vs $1/T$ and are 0.94(2), 0.57(1), and 1.51(3) eV, respectively. The changes in slope indicate variation in the conduction behavior as temperature is increased. This could arise from structural transitions or from a change in the dominant conduction mechanism. Since no crystallographic phase transitions were observed by variable-temperature diffraction, the changes in slope in the conductivity plot are more likely due to changes in the dominant charge carriers.

We also measured the conductivity of SSZ40GO under dry and wet flowing N_2. The results are summarized in Figure 2b. Above ∼700 °C, the conductivity is the same in all the atmospheres, suggesting that SSZ40GO is a purely oxide ion conductor in the high-temperature regime. In the intermediate- and low-temperature regions the conductivity in dry atmospheres is significantly lower than that in moist atmospheres. This, and the curvature of the moist-atmosphere plots, are suggestive of the presence of proton conductivity (with a magnitude comparable to the Gd-doped $BaZrO_3$, $SrZrO_3$, and $SrCeO_3$ proton conductors[35]). Similar behavior has been reported for the related Ga-rich perovskite $Sr_2Sc_{0.5}Ga_{1.5}O_5{\cdot}0.13H_2O$.[6] The conductivity behavior under air or wet N_2 can be understood in terms of a low-temperature proton-conducting region, a decreasing proton contribution at intermediate temperature as water is lost under heating, and a purely oxide ion conducting region at high temperature once all water has been lost from the sample. The difference in low-temperature conductivity between air and water-saturated N_2 is small, indicating similar water uptake under these conditions. Also, the absence of hysteresis in the heating and cooling cycles in moist N_2 suggests that SSZ40GO picks up water very quickly on cooling and starting from high temperatures (∼700 °C).

To directly compare only the oxide ion conductivity of SSGO and the zinc-substituted phases, their conductivities under dry nitrogen are plotted in Figure 2c. SSZ40GO is a better oxide ion conductor than SSGO across the entire temperature range but has a larger activation energy, possibly due to cation disorder and/or defect trapping.[36] The low- and intermediate-temperature oxide ion conductivity of SSZ40GO is lower than that of the 5%-substituted material (SSZ05GO), despite SSZ40GO having a higher symmetry, more disordered structure, and more oxygen vacancies. This again suggests the presence of local ordering that traps oxide ions. Comparisons between the conductivity curves obtained in wet and dry atmospheres show an approximately 1/2 an order of magnitude increase due to proton conductivity in SSGO and SSZ05GO. SSZ40GO shows a much larger increase (∼3 orders of magnitude, Figure 2c), suggesting that either there are more protons present or they are much more mobile.

In comparison with other families where the conductivity mechanism is well established, the oxide ion conductivity of SSZ40GO at 800 °C (1.3×10^{-4} S cm^{-1}) is around 2 orders of magnitude lower than the benchmark vacancy-type conductor yttria-stabilized zirconia[37] and also $Bi_{46}V_8O_{89}$.[38] The latter exhibits a complex oxide ion migration mechanism reliant on vacancy hopping through the fluorite-related Bi−O sublattice and fast oxide ion exchanges with the V−O sublattice.[38,39] It is also about 2 orders of magnitude lower than the oxygen-excess apatite-type $Bi_2La_8(GeO_4)_6O_3$, in which the ionic migration proceeds mainly via interstitial oxygen exchanges between GeO_4 and GeO_5 groups, with a smaller contribution from diffusion along the hexagonal channels in the structure,[40−42] and 1 order of magnitude lower than oxygen-excess scheelite-type $LaNb_{0.92}W_{0.08}O_{4.04}$.[43,44] It compares favorably with perovskite-related $Nd_{0.9}Sr_{0.1}BaInO_{3.95}$, which exhibits strongly anisotropic vacancy-hopping-based oxide ion diffusion.[45]

https://dx.doi.org/10.1021/acs.chemmater.0c01378
Chem. Mater. 2020, 32, 4347−4357

While SSZ40GO is therefore a moderately good oxide ion conductor in absolute terms, the most significant direct comparison is the 2 orders of magnitude oxide ion conductivity increase relative to its parent compound SSGO, likely related to the changes of local structure described later in the paper.

Water Incorporation into $SrSc_{0.3}Zn_{0.2}Ga_{0.5}O_{2.4}$. To support the conclusion of a proton conductivity contribution in SSZ40GO, its water uptake was probed with a variety of methods. ^{1}H NMR showed a weak resonance at 3.1 ppm, indicating the presence of a small number of protons. TGA measurements showed two regions of mass loss: between 100 and 400 °C and at 700−800 °C. Multiple TGA measurements (Figure S5) on different SSZ40GO samples gave a formula of $SrSc_{0.3}Zn_{0.2}Ga_{0.5}O_{2.4}{\cdot}xH_2O$, with x between 0.025 and 0.1, depending on the exact thermal history of the sample.

Unit cell parameters extracted from VT-XRD also show a deviation from their extrapolated high-temperature behavior between 100 and 400 °C (Figure 3). This is more apparent in the derived thermal expansion coefficient, which also reveals a smaller change at ∼800 °C. These discontinuities coincide with the mass losses in the TGA and are therefore likely to be due to the same process. They are also consistent with the moist-atmosphere impedance data, where we proposed the proton contribution starts decreasing above ∼300 °C and disappears completely from 800 °C.

On first inspection there is an apparent discrepancy between the TGA data, which show no, or very limited, water uptake on cooling on the time scale of the experiment (∼100 min, Figure 3c) and the conductivity data which suggest rapid water uptake even at high temperature (Figure 2b). Interestingly, the VT-XRD data show both behaviors, depending on how the experiment is conducted. When data are recorded on loosely sprinkled powder sample on heating and cooling, the cell parameter changes are irreversible, suggesting no moisture uptake on cooling, even at the very slow cooling rate of 0.1 K min^{-1}. In contrast, when data are recorded on a pressed pellet (similar to those used for impedance measurements), we see clear reversible cell parameter behavior, suggesting moisture uptake below 300 °C. Unit cell parameter changes illustrating the reversible and irreversible behavior are given in Figure S6. Our diffraction and impedance experiments therefore consistently show that pelletized samples undergo reversible water uptake, whereas loose powders show little or very slow water uptake. This can be rationalized in terms of the enhanced capillary effects caused by the concave pores on the surface of the pellet versus the convex surface of the loose powder grains.[46−50]

Probing Dynamics in $SrSc_{0.3}Zn_{0.2}Ga_{0.5}O_{2.4}$ by Inelastic Neutron Scattering. Inelastic neutron scattering data were collected on SSZ40GO on the time-of-flight spectrometer IN6-SHARP to probe dynamics on picosecond time scales. QENS spectra were recorded at 20, 200, 400, 600, 800, and 1000 °C. Plots of the scattering function $S(Q = 1.92, \omega)$ against energy transfer are shown in Figure 4a and as color maps of $S(Q,\omega)$ in Figure 4b. The appearance of a QENS signal at high temperatures is evident from the broadening of the elastic peak between 800 and 1000 °C (red and orange curves in Figure 4a, respectively). Figure 4b shows that this broadening is largest at high Q values.

This indicates the onset of a high-temperature dynamic process in SSZ40GO on the picosecond time scale. To demonstrate that this process corresponds to long-range jump diffusion and calculate jump distance and lifetime, we considered the Q dependence of the QENS signal (Figure S7). However, the data quality at low Q values precludes us from drawing a definitive conclusion. While picosecond dynamics are observed in SSZ40GO, we did not record clear QENS broadening signals at a sufficient number of temperatures to allow us to extract quantitative parameters such as the activation energy for this process.

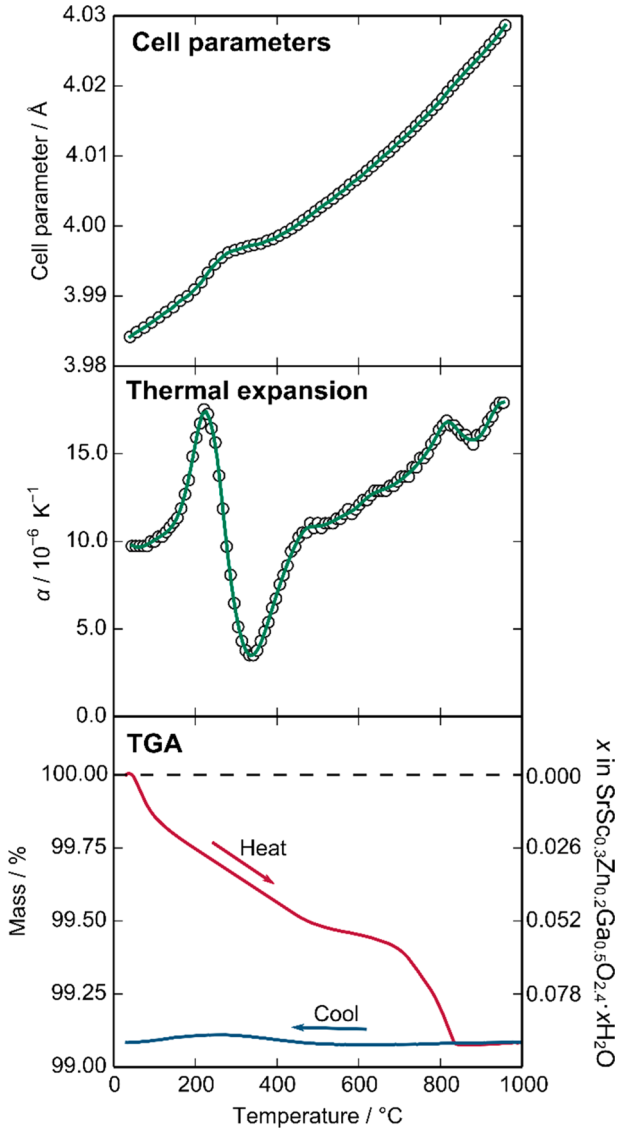

Figure 3. SSZ40GO cell parameter evolution with temperature from variable temperature X-ray diffraction (top panel) and derived thermal expansion ($d\alpha/dT$) (middle). Thermogravimetric analysis over the same temperature range (bottom) on both heating and cooling cycles. Cell parameters on cooling are shown in the Supporting Information.

The phonon density of states (PDOS) plots extracted from the spectra measured at 20, 200, 400, 600, 800, and 1000 °C are shown in Figure S8. The most prominent change is the disappearance of a broad feature centered around 80 meV between 200 and 400 °C. This broad band in the INS spectra corresponds to librational motions of water molecules.[51,52] Water loss in SSZ40GO in this temperature range is consistent with the conductivity, unit cell parameter, and TGA observations discussed above.

https://dx.doi.org/10.1021/acs.chemmater.0c01378
Chem. Mater. 2020, 32, 4347−4357

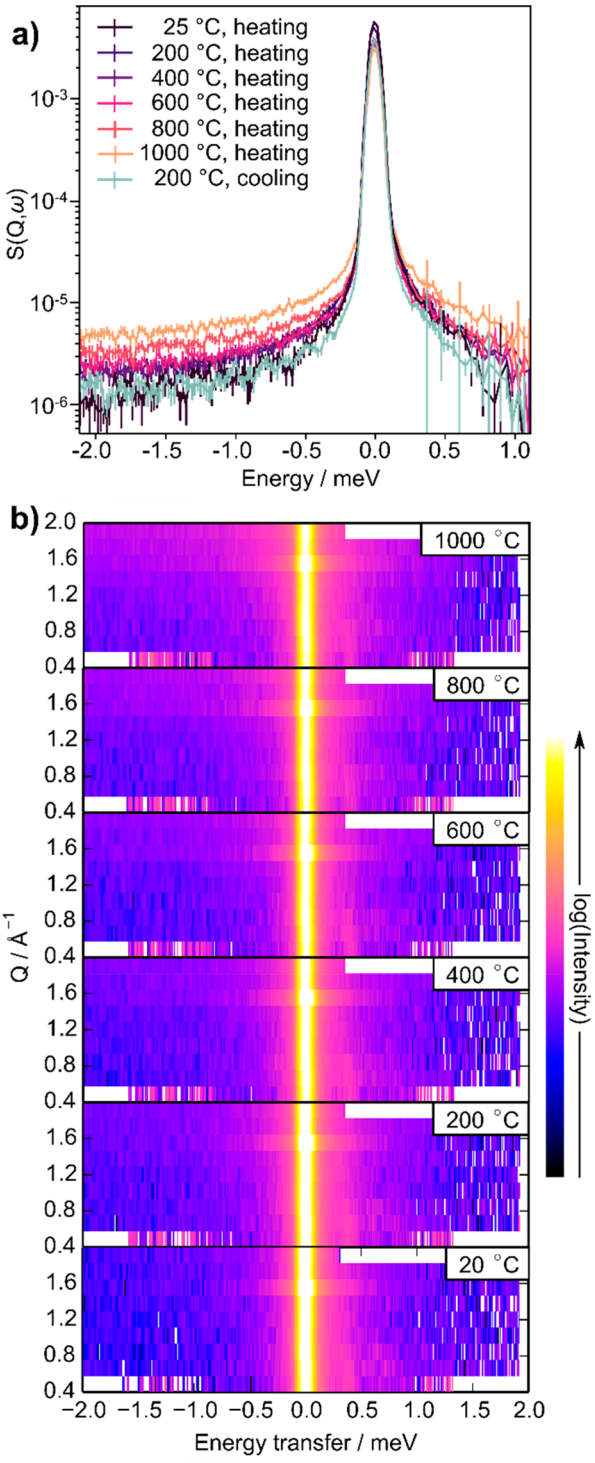

Figure 4. (a) Plot of the scattering function $S(\omega)$ at Q = 1.92 Å showing the QENS broadening of the elastic peak. (b) Color maps of $S(Q,\omega)$ at different temperatures to show the evolution of the QENS broadening at high temperatures and that this is enhanced at high Q.

Elastic and inelastic fixed window scans performed on the backscattering spectrometer IN16B, which is sensitive to motions on the nanosecond time scale, are shown in Figures 5a and 5b, respectively. These measurements record the intensity of the elastic peak (at 0 μeV) and the inelastic intensity at fixed energy offset as a function of temperature. An inelastic energy offset of 2 μeV was chosen based on our previous measurements of mixed metal oxide systems.[53]

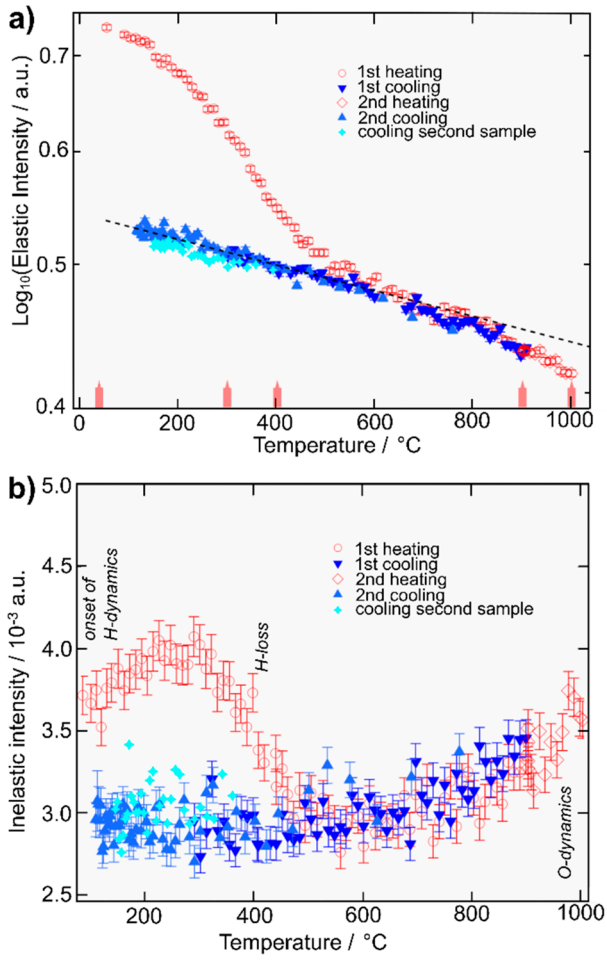

Figure 5. (a) Elastic intensity as a function of temperature summed over all Q values (0.2−1.75 Å^{-1}). Multiple heating and cooling cycles are shown. The dashed line is a guide to the eye showing the expected decrease in intensity due to Debye−Waller effects. Temperatures where QENS spectra were subsequently measured are indicated by the red markers on the temperature axis. (b) Inelastic intensity at 2 μeV energy transfer as a function of temperature summed over all Q values (0.2−1.75 Å^{-1}). Key features are labeled with the dynamic processes to which they have been attributed.

On heating, we see a decrease of ∼30% in the elastic intensity up to 500 °C. This is a steeper decrease in intensity than would be expected due to Debye−Waller effects alone. This can be seen from the shallower gradient at higher temperatures on heating and on cooling (dashed line in the EFWS in Figure 5a). This loss of elastic intensity coincides with a peak in the inelastic fixed window scans. Together, these data suggest a dynamic process occurring in SSZ40GO at these lower temperatures, which is irreversible on cooling in vacuum. Based on our other experimental evidence, this dynamic process likely arises from the mobility of protons and the subsequent water loss. A second decrease of the elastic intensity and concurrent increase in the inelastic intensity at 2 μeV is observed from 600 °C onward (Figure 5b). This can be attributed to oxide ion dynamics which dominate the conductivity at high temperatures.

Full inelastic spectra measured on the IN16B spectrometer after the initial sample heating (i.e., after water had been removed from the sample) are shown in Figure S9. As expected, no QENS signals were seen in the lower temperature

https://dx.doi.org/10.1021/acs.chemmater.0c01378
Chem. Mater. 2020, 32, 4347−4357

region. Only a weak indication of broadening was observed at the highest temperature in our experiment (1000 °C, red vs blue data points in the bottom panel of Figure S9), despite the increase in inelastic intensity indicating that the dynamics have entered the energy window of the instrument. In other words, the second dynamic process, corresponding to oxide ion conduction, is either too fast or too weak at 1000 °C to be unambiguously and reliably observed from IN16B data.

It is worth noting that in this study we observed oxide ion dynamics directly by neutron scattering for SSZ40GO, while they were not observed for SSGO on either IN6-SHARP or IN16B.[5] This is consistent with impedance measurements, which show that oxide ion conductivity of SSZ40GO at high temperatures (2.9×10^{-2} S cm^{-1} at 900 °C) is about 2 orders of magnitude higher than that of undoped SSGO (3×10^{-4} S cm^{-1} at 900 °C). These findings are also consistent with our neutron scattering study of $La_2Mo_2O_9$, which exhibits oxide ion conductivity of 2×10^{-2} S cm^{-1} at 600 °C (i.e., the same order of magnitude as SSZ40GO at 900 °C), where QENS signals were observed on IN16B from 570 °C onward.[54]

Local Structure of $SrSc_{0.3}Zn_{0.2}Ga_{0.5}O_{2.4}$. Powder X-ray and neutron diffraction show that SSZ40GO is a disordered perovskite on average, but from a chemical perspective we expect there to be significant local ordering due to the different coordination preferences of the cations, the large number of oxygen vacancies relative to the ABO_3 perovskite, and the diffuse scattering seen in the NPD pattern. In addition, ^{45}Sc and ^{71}Ga solid-state NMR spectra (Figure S10) suggest that both species are present in a range of local environments.

The local structure was studied in more detail using neutron total scattering and PDF analysis. As a starting point, an average perovskite model was fitted to the Bragg and PDF data simultaneously, yielding the $D(r)$ fit shown in Figure 6a. The $D(r)$ data at large r are described fairly well by the perovskite model, but there are significant deviations below ~8 Å. Since these features could not be described using a simple perovskite unit cell, a series of large-box models were tested. In each case, an approximately isotropic simulation box containing 2000–8000 atoms was created. Topas Academic was used to fit the atomic coordinates of the models to the PDF and Bragg data simultaneously, subject to polyhedral restraints to maintain sensible local chemical environments. By including the Bragg data, the local structural model remains consistent with the average long-range structure. Models were judged based on the visual fits to both data sets and the corresponding R-factors, alongside coordination number, bond length, and bond angle distributions that assess chemical plausibility.

The closely related brownmillerite structural model was tested first. All Sc atoms were placed on the octahedral sites, occupying 60% of them. The remaining 40% of octahedral sites and the tetrahedral sites were populated by Ga and Zn in their nominal ratios. This distribution reflects the coordination environment preferences of the atoms based on the statistical analysis by Waroquiers et al.[55] and what would be expected based on related oxides. The calculated $D(r)$ shows significant differences to the experimental data, but the positions of the first two peaks are well-described (Figure 6b). Here, the shorter bond lengths at ~1.85 Å come from tetrahedra and the longer bonds at ~2.05 Å from octahedra. This suggests that SSZ40GO contains these (or similar) polyhedral units. The octahedral:tetrahedral group ratio (Oh:T) in brownmillerite is 1:1, and this (when combined with the different scattering lengths) overestimates the peak due to the longer, octahedral

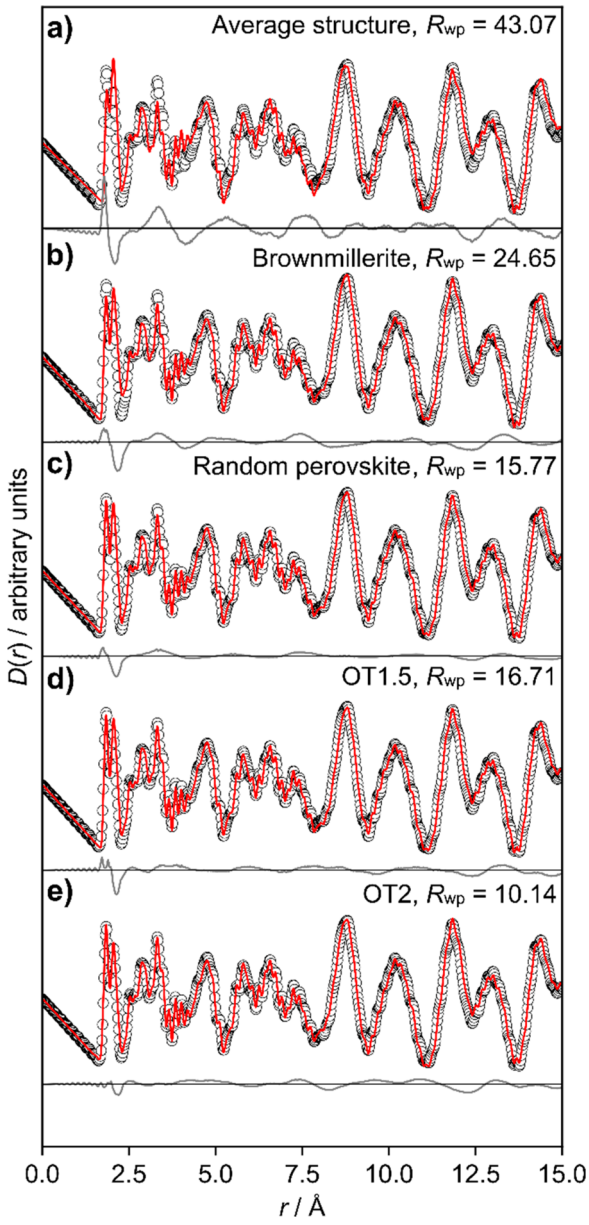

Figure 6. Fit of various local structure models (red curve) to the measured PDF (black markers) data of SSZ40GO. Difference curves are shown in gray. The R_{wp} values given are calculated for 1.5 Å ≤ r ≤ 8 Å to reflect the fit to the local structure.

bonds compared to the experimental data. This calculated overestimate relative to the experimental data implies that SSZ40GO must contain more tetrahedral than octahedral groups, and therefore more of the Zn and Ga occupy tetrahedral sites.

The next model tested therefore aimed to maximize the number of tetrahedra while retaining the polyhedral corner connectivity of the brownmillerite and perovskite structures. An in-house Monte Carlo code was used to construct the polyhedral framework. Starting from a perovskite structure, oxygen atoms were randomly removed to produce an oxygen content corresponding to $ABO_{2.4}$; oxygen atoms and vacancies were then swapped to create a network of chemically sensible corner-linked polyhedra. The numbers of 1-, 2-, 3-, and 5-coordinate polyhedra were minimized by the algorithm, and the resulting configuration comprised 60% 4-coordinate

https://dx.doi.org/10.1021/acs.chemmater.0c01378
Chem. Mater. 2020, 32, 4347–4357

polyhedra, 39% octahedra, and 1% 5-coordinate polyhedra, with a ratio of octahedra to 4-coordinate polyhedra of 1:1.5. One consequence of this minimization algorithm is the creation of square-planar sites alongside tetrahedra (~20% of the 4-coordinate sites; the statistically expected number). This is somewhat undesirable as none of the B-site cations are expected to occupy square-planar environments but is difficult to avoid. (Configurations in which we explicitly minimized the number of square-planar sites had a higher number of 1-, 2-, and 3-coordinate polyhedra, which is chemically less likely.) After the construction of the polyhedral network, cations were initially arranged randomly across all sites to give the correct overall composition.

This model gave a good fit to the data both locally and on longer length scales; however, it is not chemically sensible as the cations do not have their preferred coordination environment.[55] For example, analysis of 103 Sc-containing compounds by Waroquiers et al.[55] found no occurrences of 4-coordinate Sc so we can be confident that this random model is not a likely representation of the real structure. When a more sensible cation distribution was imposed, i.e., Sc atoms were exclusively placed on octahedral sites and Ga and Zn were arranged over the remaining octahedral and 4-coordinate sites, the local fit became significantly worse with the model again overestimating the peak due to 2.05 Å bond lengths (see Figure 6c).

These observations suggest that SSZ40GO contains more tetrahedral groups than the Oh:T ratio 1:1.5 indicates. The only way to attain this with the oxygen content $ABO_{2.4}$ or $ABO_{2.5}$ is to break the corner connectivity of the polyhedra and include some with one-coordinate or terminal oxygen sites (e.g., $MO_{3/2}O_1$ tetrahedral groups in Niggli formalism). A small number of perovskite-related compounds with such units have been reported. The compound $Sr_{10}Sc_4Ga_6O_{25}$ described by Chernov et al.[6] has an Oh:T ratio of 1:1.5 in which one-third of the tetrahedra have terminal O sites ($MO_{3/2}O_1$). Several compounds with general formula $A_3Oh_1T_2O_{7.5}$ (where A = Ba, Sr, Na, Ca; Oh = Y, Mn, Er; and T = Ga, Co, V, Al, Si)[56−61] have a Oh:T ratio of 1:2, with half the tetrahedra being $MO_{3/2}O_1$. Structures of $Sr_{10}Sc_4Ga_6O_{25}$ and $Ba_3ErGa_2O_{7.5}$ are included as examples in Figure S11. The compound $Sr_2Sc_{0.5}Ga_{1.5}O_5$, also reported by Chernov,[6] is proposed to have an even higher tetrahedron content (Oh:T of 1:3), although its structure was simply reported as a disordered perovskite.

Large box models corresponding to $A_2Oh_{0.8}T_{1.2}O_5$ (OT1.5) and $A_2Oh_{0.66}T_{1.33}O_5$(OT2) were constructed based on these literature structures[6,56] and fitted to the PDF and Bragg data of SSZ40GO. Both models provide a good description of the local structure below 8 Å. OT1.5 still slightly overestimates the proportion of the 2.05 Å bond lengths (Figure 6d), whereas OT2 gives a much better agreement (Figure 6e). The close agreement between this final model and the observed data suggests that terminal oxygen sites are present in SSZ40GO. Distributions of bond length and angles of the final model are available in Figure S12.

It is of course possible that there are some 5-coordinate species present in SSZ40GO. This has been suggested, for example, in structural models of disordered $BaY_{0.25}Fe_{0.75}O_{2.5}$.[62] Although Zn and Ga do not have the strong electronic driving force for 5-coordination exhibited by some transition metals, 5-coordination is found in some of their oxides. It is, however, significantly less common than 4- or 6-coordination; Waroquiers et al. give values of 48%:21%:20% and 61%:6%:33% 4:5:6 for Zn and Ga, respectively.[55] This tendency is also reflected in molecular compounds. The 2020 Cambridge Structural Database[63] shows a ~40%:20%:40% ratio of 4:5:6 coordination for Zn coordinated solely by O and a 30%:10%:60% ratio for Ga. We also tested two structural models containing more 5-coordinate metal sites (a random perovskite model with a 39%:42%:19% 4:5:6 coordination number ratio and the favored $Ba_3YFe_2O_{7.5}$ model of King et al.[62] with 25%:25%:50% Td:SqPy:Oh, both with the 6-coordinate sites being exclusively occupied by Sc and Zn/Ga on other sites); both models gave significantly worse fits to the data. Given the complexity of SSZ40GO and the fact that the contributions from all the M−O distances contribute to a relatively narrow region of the PDF, it is not possible to definitively rule out the possibility of a small number of five-coordinate Zn/Ga, but we favor our all octahedral−tetrahedral model.

There is a very small overestimation of the peak due to 2.05 Å bonds in our final OT2 model, but this is likely to be due to the fact that the model has an oxygen stoichiometry of $O_{2.5}$ (normalized to perovskite) whereas SSZ40GO has $O_{2.4}$. This could mean that the real material has an even higher proportion of tetrahedra. Indeed, if all Ga and Zn atoms in SSZ40GO occupied a tetrahedral site, the Oh:T ratio would be 1:2.33, but we are not aware of a simple perovskite derivative structure corresponding to this composition. Polyhedral connectivity leading to an Oh:T ratio of 1:3, as would be expected in the single-phase limit SSZ50GO, is geometrically possible; however, we are again unaware of structurally characterized compounds with this ratio. The local structure of the closely related compound, $Sr_2Sc_{0.5}Ga_{1.5}O_5$, has not been fully investigated, but evidence of local ordering was observed as diffuse scattering in electron diffraction patterns[6] indicating that small domains of this connectivity may be plausible. This material was also shown to decompose in moist atmospheres, suggesting this connectivity pattern is very not stable.

The final OT2 model was also fitted to data sets recorded at 600 and 1000 °C. No major structural changes are expected relative to room temperature since the diffraction patterns show no phase transitions. The structural diffuse scattering in the NPD pattern is also unchanged up to at least 900 °C, so it is unlikely that the local structure undergoes significant changes. We find that, with the exception of thermal broadening, the experimental PDFs at higher temperatures are comparable with that at room temperature. Accordingly, the OT2 model gives a good fit to both the 600 and 1000 °C data sets (Figure S13).

4. CONCLUSIONS

We have investigated Zn substitution for Sc in Sr_2ScGaO_5, resulting in the formation of a new *Pm*-3*m* perovskite phase for certain Zn concentrations. The composition $SrSc_{0.3}Zn_{0.2}Ga_{0.5}O_{2.4}$ (SSZ40GO) was studied in detail. This phase is a highly disordered perovskite on average, has a remarkably low oxygen content, and shows a two order of magnitude increase in conductivity over its brownmillerite parent at high temperature. It can incorporate a limited amount of water reversibly into the structure, resulting in a measurable change in low-temperature cell parameters as well as a significant proton contribution to the conductivity. QENS signals were observed for both proton and oxygen dynamics, but they were not large enough to extract quantitative

https://dx.doi.org/10.1021/acs.chemmater.0c01378
Chem. Mater. 2020, 32, 4347−4357

parameters such as activation energy, jump length, and frequency.

The local structure of SSZ40GO is markedly different from its average structure. Large-box fitting to neutron total scattering data suggests that local polyhedral environments include 50% of the tetrahedra with a terminal oxygen site. The terminal oxygen site is an unusual structural feature but consistent with observations in related crystallographically characterized materials. There is significant precedence from our work and that of others that this type of low-linked tetrahedron can lead to oxygen dynamics at low temperatures,[7−10] and this could be a contributing factor to why SSZ40GO has a higher oxide ion conductivity than its parent material, SSGO, by two orders of magnitude.

■ ASSOCIATED CONTENT

Supporting Information

The Supporting Information is available free of charge at https://pubs.acs.org/doi/10.1021/acs.chemmater.0c01378.

Diffraction patterns of all synthesized compounds; variable temperature XRD on SSZ40GO; additional variable temperature NPD patterns of SSZ40GO; a representative complex impedance plot; TGA and cell parameter cycling plots; Q dependence of the QENS signals from IN6; phonon density of states of SSZ40GO from IN6; inelastic spectra from IN16B; comparison of NMR signals between SSGO and SSZ40GO; depictions of the discussed structures with increasing Oh:T ratio; Bragg fit and structural analysis of the final OT2 local structure model and high-temperature local structure fits (PDF)

■ AUTHOR INFORMATION

Corresponding Author

Ivana Radosavljevic Evans − *Department of Chemistry, Durham University, Durham DH1 3LE, U.K.;* orcid.org/0000-0002-0325-7229; Email: ivana.radosavljevic@durham.ac.uk

Authors

Chloe A. Fuller − *Department of Chemistry, Durham University, Durham DH1 3LE, U.K.*

Quentin Berrod − *CNRS, CEA, IRIG-SyMMES, Université Grenoble Alpes, 38000 Grenoble, France; Institut Laue Langevin, 38000 Grenoble, France;* orcid.org/0000-0003-3254-1779

Bernhard Frick − *Institut Laue Langevin, 38000 Grenoble, France*

Mark R. Johnson − *Institut Laue Langevin, 38000 Grenoble, France*

Maxim Avdeev − *Australian Nuclear Science and Technology Organisation, Lucas Heights, NSW 2234, Australia;* orcid.org/0000-0003-2366-5809

John S. O. Evans − *Department of Chemistry, Durham University, Durham DH1 3LE, U.K.;* orcid.org/0000-0001-6305-6341

Complete contact information is available at: https://pubs.acs.org/10.1021/acs.chemmater.0c01378

Notes

The authors declare no competing financial interest.

■ REFERENCES

(1) Adler, S. B.; Baltisberger, J.; Werner, U.; Reimer, J. A. Chemical Structure and Oxygen Dynamics in $Ba_2In_2O_5$. *J. Am. Chem. Soc.* **1994**, *116* (2), 675−681.

(2) Ishihara, T.; Matsuda, H.; Takita, Y. Doped $LaGaO_3$ Perovskite Type Oxide as a New Oxide Ionic Conductor. *J. Am. Chem. Soc.* **1994**, *116* (9), 3801−3803.

(3) Li, M.; Pietrowski, M. J.; De Souza, R. A.; Zhang, H.; Reaney, I. M.; Cook, S. N.; Kilner, J. A.; Sinclair, D. C. A Family of Oxide Ion Conductors Based on the Ferroelectric Perovskite $Na_{0.5}Bi_{0.5}TiO_3$. *Nat. Mater.* **2014**, *13* (1), 31−35.

(4) Corallini, S.; Ceretti, M.; Cousson, A.; Ritter, C.; Longhin, M.; Papet, P.; Paulus, W. Cubic Sr_2ScGaO_5 Perovskite: Structural Stability, Oxygen Defect Structure, and Ion Conductivity Explored on Single Crystals. *Inorg. Chem.* **2017**, *56* (5), 2977−2984.

(5) Fuller, C. A.; Berrod, Q.; Frick, B.; Johnson, M. R.; Clark, S. J.; Evans, J. S. O.; Evans, I. R. Brownmillerite-Type Sr_2ScGaO_5 Oxide Ion Conductor: Local Structure, Phase Transition, and Dynamics. *Chem. Mater.* **2019**, *31* (18), 7395−7404.

(6) Chernov, S. V.; Dobrovolsky, Y. A.; Istomin, S. Y.; Antipov, E. V.; Grins, J.; Svensson, G.; Tarakina, N. V.; Abakumov, A. M.; Van Tendeloo, G.; Eriksson, S. G.; et al. Sr_2GaScO_5, $Sr_{10}Ga_6Sc_4O_{25}$, and $SrGa_{0.75}Sc_{0.25}O_{2.5}$: A Play in the Octahedra to Tetrahedra Ratio in Oxygen-Deficient Perovskites. *Inorg. Chem.* **2012**, *51* (2), 1094−1103.

(7) Kendrick, E.; Islam, M. S.; Slater, P. R. Developing Apatites for Solid Oxide Fuel Cells: Insight into Structural, Transport and Doping Properties. *J. Mater. Chem.* **2007**, *17* (30), 3104−3111.

(8) Evans, J. S. O.; Hu, Z.; Jorgensen, J. D.; Argyriou, D. N.; Short, S.; Sleight, A. W. Compressibility, Phase Transitions, and Oxygen Migration in Zirconium Tungstate, ZrW_2O_8. *Science (Washington, DC, U. S.)* **1997**, *275* (5296), 61−65.

(9) Kuang, X.; Green, M. A.; Niu, H.; Zajdel, P.; Dickinson, C.; Claridge, J. B.; Jantsky, L.; Rosseinsky, M. J. Interstitial Oxide Ion Conductivity in the Layered Tetrahedral Network Melilite Structure. *Nat. Mater.* **2008**, *7*, 498−504.

(10) Tallentire, S. E.; Child, F.; Fall, I.; Vella-Zarb, L.; Evans, I. R.; Tucker, M. G.; Keen, D. A.; Wilson, C.; Evans, J. S. O. Systematic and Controllable Negative, Zero, and Positive Thermal Expansion in Cubic $Zr_{1-x}Sn_xMo_2O_8$. *J. Am. Chem. Soc.* **2013**, *135*, 12849−12856.

(11) Rietveld, H. M. A Profile Refinement Method for Nuclear and Magnetic Structures. *J. Appl. Crystallogr.* **1969**, *2* (2), 65−71.

(12) Coelho, A.; Evans, J. S. O.; Evans, I. R.; Kern, A.; Parsons, S. The TOPAS Symbolic Computation System. *Powder Diffr.* **2011**, *26*, 22−25.

(13) Leineweber, A.; Dinnebier, R.; Evans, J. S. O. *Rietveld Refinement, Practical Powder Diffraction Pattern Analysis Using TOPAS.*; De Gruyter: Berlin, 2018.

(14) Stinton, G. W.; Evans, J. S. O. Parametric Rietveld Refinement. *J. Appl. Crystallogr.* **2007**, *40* (1), 87−95.

(15) Avdeev, M.; Hester, J. R. ECHIDNA: A Decade of High-Resolution Neutron Powder Diffraction at OPAL. *J. Appl. Crystallogr.* **2018**, *51* (6), 1597−1604.

(16) O'Dell, L. A.; Schurko, R. W. QCPMG Using Adiabatic Pulses for Faster Acquisition of Ultra-Wideline NMR Spectra. *Chem. Phys. Lett.* **2008**, *464* (1−3), 97−102.

(17) Soper, A. K. GudrunN and GudrunX: Programs for Correcting Raw Neutron and X-Ray Diffraction Data to Differential Scattering Cross Section. Rutherford Applet. Lab. Technol. Rep. RAL-TR-2011-013, 2011.

(18) Keen, D. A. A Comparison of Various Commonly Used Correlation Functions for Describing Total Scattering. *J. Appl. Crystallogr.* **2001**, *34* (2), 172−177.

(19) Arnold, O.; Bilheux, J. C.; Borreguero, J. M.; Buts, A.; Campbell, S. I.; Chapon, L.; Doucet, M.; Draper, N.; Ferraz Leal, R.; Gigg, M. A.; et al. Mantid—Data Analysis and Visualization Package for Neutron Scattering and μ SR Experiments. *Nucl. Instrum. Methods Phys. Res., Sect. A* **2014**, *764*, 156−166.

(20) Frick, B.; Combet, J.; Van Eijck, L. New Possibilities with Inelastic Fixed Window Scans and Linear Motor Doppler Drives on

High Resolution Neutron Backscattering Spectrometers. *Nucl. Instrum. Methods Phys. Res., Sect. A* **2012**, *669*, 7−13.
(21) Richard, D.; Ferrand, M.; Kearley, J. LAMP, the Large Array Manipulation Program. *J. Neutron Res.* **1996**, *4*, 33−39.
(22) Zanotti, J.-M. *QENSH*, 2018, http://iramis.cea.fr/llb/Phocea/Page/index.php?id=21.
(23) Speakman, S. A.; Richardson, J. W.; Mitchell, B. J.; Misture, S. T. In-Situ Diffraction Study of $Ba_2In_2O_5$. *Solid State Ionics* **2002**, *149* (3−4), 247−259.
(24) Shin, S.; Yonemura, M.; Ikawa, H. Order-Disorder Transition of $Sr_2Fe_2O_5$ from Brownmillerite to Perovskite Structure at an Elevated Temperature. *Mater. Res. Bull.* **1978**, *13* (10), 1017−1021.
(25) Dong, F.; Chen, Y.; Chen, D.; Shao, Z. Surprisingly High Activity for Oxygen Reduction Reaction of Selected Oxides Lacking Long Oxygen-Ion Diffusion Paths at Intermediate Temperatures: A Case Study of Cobalt-Free $BaFeO_{3-\Delta}$. *ACS Appl. Mater. Interfaces* **2014**, *6* (14), 11180−11189.
(26) Kuklja, M. M.; Kotomin, E. A.; Merkle, R.; Mastrikov, Y. A.; Maier, J. Combined Theoretical and Experimental Analysis of Processes Determining Cathode Performance in Solid Oxide Fuel Cells. *Phys. Chem. Chem. Phys.* **2013**, *15*, 5443−5471.
(27) Istomin, S. Y.; Antipov, E.V.; Svensson, G.; Attfield, J.P.; Kozhevnikov, V.L.; Leonidov, I.A.; Patrakeev, M.V.; Mitberg, E.B. A Novel Complex Cobalt Gallium Oxide $Ca_2Co_{0.8}Ga_{1.2}O_{4.8}$: Synthesis and High-Temperature Electron Transport Properties. *J. Solid State Chem.* **2002**, *167*, 196−202.
(28) Waidha, A. I.; Zhang, H.; Lepple, M.; Dasgupta, S.; Alff, L.; Slater, P.; Fortes, A. D.; Clemens, O. $BaCoO_{2+\delta}$: A New Highly Oxygen Deficient Perovskite-Related Phase with Unusual Co Coordination Obtained by High Temperature Reaction with Short Reaction Times. *Chem. Commun.* **2019**, *55* (20), 2920−2923.
(29) Mentré, O.; Iorgulescu, M.; Huvé, M.; Kabbour, H.; Renaut, N.; Daviero-Minaud, S.; Colis, S.; Roussel, P. $BaCoO_{2.22}$: The Most Oxygen-Deficient Certified Cubic Perovskite. *Dalt. Trans.* **2015**, *44* (23), 10728−10737.
(30) Takano, M.; Takeda, Y.; Okada, H.; Miyamoto, M.; Kusaka, T. $ACuO_2$(A: Alkaline Earth) Crystallizing in a Layered Structure. *Phys. C* **1989**, *159* (4), 375−378.
(31) Tsujimoto, Y.; Tassel, C.; Hayashi, N.; Watanabe, T.; Kageyama, H.; Yoshimura, K.; Takano, M.; Ceretti, M.; Ritter, C.; Paulus, W. Infinite-Layer Iron Oxide with a Square-Planar Coordination. *Nature* **2007**, *450* (7172), 1062−1065.
(32) Crespin, M.; Levitz, P.; Gatineau, L. Reduced Forms of $LaNiO_3$ Perovskite. Part 1.—Evidence for New Phases: $La_2Ni_2O_5$ and $LaNiO_2$. *J. Chem. Soc., Faraday Trans. 2* **1983**, *79* (8), 1181−1194.
(33) Takeda, Y.; Imanishi, N.; Kanno, R.; Mizuno, T.; Higuchi, H.; Yamamoto, O.; Takano, M. Oxide Ion Conductivity in Perovskite Type Sr_2ScAlO_5 and Related Compounds. *Solid State Ionics* **1992**, *53*−*56*, 748−753.
(34) Irvine, J. T. S.; Sinclair, D. C.; West, A. R. Electroceramics: Characterization by Impedance Spectroscopy. *Adv. Mater.* **1990**, *2*, 132−138.
(35) Zając, W.; Rusinek, D.; Zheng, K.; Molenda, J. Applicability of Gd-Doped $BaZrO_3$, $SrZrO_3$, $BaCeO_3$ and $SrCeO_3$ Proton Conducting Perovskites as Electrolytes for Solid Oxide Fuel Cells. *Cent. Eur. J. Chem.* **2013**, *11* (4), 471−484.
(36) Perriot, R.; Uberuaga, B. P. Structural vs. Intrinsic Carriers: Contrasting Effects of Cation Chemistry and Disorder on Ionic Conductivity in Pyrochlores. *J. Mater. Chem. A* **2015**, *3* (21), 11554−11565.
(37) León-Reina, L.; Losilla, E. R.; Martínez-Lara, M.; Martín-Sedeño, M. C.; Bruque, S.; Núñez, P.; Sheptyakov, D. V.; Aranda, M. A. G. High Oxide Ion Conductivity in Al-Doped Germanium Oxyapatite. *Chem. Mater.* **2005**, *17* (3), 596−600.
(38) Kuang, X.; Payne, J. L.; Farrell, J. D.; Johnson, M. R.; Evans, I. R. Polymorphism and Oxide Ion Migration Pathways in Fluorite-Type Bismuth Vanadate, $Bi_{46}V_8O_{89}$. *Chem. Mater.* **2012**, *24*, 2162−2167.
(39) Dunstan, M. T.; Halat, D. M.; Tate, M. L.; Evans, I. R.; Grey, C. P. Variable-Temperature Multinuclear Solid-State NMR Study of Oxide Ion Dynamics in Fluorite-Type Bismuth Vanadate and Phosphate Solid Electrolytes. *Chem. Mater.* **2019**, *31* (5), 1704−1714.
(40) Tate, M. L.; Blom, D. A.; Avdeev, M.; Brand, H. E. A.; McIntyre, G. J.; Vogt, T.; Evans, I. R. New Apatite-Type Oxide Ion Conductor, $Bi_2La_8(GeO_4)_6O_3$: Structure, Properties, and Direct Imaging of Low-Level Interstitial Oxygen Atoms Using Aberration-Corrected Scanning Transmission Electron Micros. *Adv. Funct. Mater.* **2017**, *27* (8), 1605625.
(41) Peet, J. R.; Piovano, A.; Johnson, M. R.; Evans, I. R. Location and Orientation of Lone Pairs in Apatite-Type Materials: A Computational Study. *Dalt. Trans.* **2017**, *46* (46), 15996−15999.
(42) Peet, J. R.; Chambers, M. S.; Piovano, A.; Johnson, M. R.; Evans, I. R. Dynamics in Bi(III)-Containing Apatite-Type Oxide Ion Conductors: A Combined Computational and Experimental Study. *J. Mater. Chem. A* **2018**, *6*, 5129−5135.
(43) Toyoura, K.; Sakakibara, Y.; Yokoi, T.; Nakamura, A.; Matsunaga, K. Oxide-Ion Conduction: Via Interstitials in Scheelite-Type $LaNbO_4$: A First-Principles Study. *J. Mater. Chem. A* **2018**, *6* (25), 12004−12011.
(44) Li, C.; Bayliss, R. D.; Skinner, S. J. Crystal Structure and Potential Interstitial Oxide Ion Conductivity of $LnNbO_4$ and $LnNb_{0.92}W_{0.08}O_{4.04}$ (Ln = La, Pr, Nd). *Solid State Ionics* **2014**, *262*, 530−535.
(45) Li, C.; Dammak, H.; Dezanneau, G. Identification of Oxygen Diffusion Mechanisms in $Nd_{1-x}AE_xBaInO_{4-x/2}$ (AE = Ca, Sr, Ba) Compounds through Molecular Dynamics. *Phys. Chem. Chem. Phys.* **2019**, *21* (38), 21506−21516.
(46) Jain, M. K.; Bhatnagar, M. C.; Sharma, G. L. Effect of Pore Size Distribution on Humidity Sensing Properties of MgO Doped ZrO_2-TiO_2 Ceramic. *Japanese J. Appl. Physics, Part 1 Regul. Pap. Short Notes Rev. Pap.* **2000**, *39* (1), 345−350.
(47) Sidhu, P. S.; Cussler, E. L. Diffusion and Capillary Flow in Track-Etched Membranes. *J. Membr. Sci.* **2001**, *182* (1−2), 91−101.
(48) Yamazoe, N.; Shimizu, Y. Humidity Sensors: Principles and Applications. *Sens. Actuators* **1986**, *10* (3−4), 379−398.
(49) Kim, S.; Merkle, R.; Maier, J. Water Uptake of Nanocrystalline Ceria: Weight and Conductance Effects. *Solid State Ionics* **2003**, *161* (1−2), 113−119.
(50) Carrott, M. R.; Carrott, P.; De Carvalho, M. B.; Sing, K. S. W. Ex-Hydroxide Magnesium Oxide as a Model Adsorbent for Investigation of Micropore Filling Mechanisms. *J. Chem. Soc., Faraday Trans.* **1991**, *87* (1), 185−191.
(51) Loong, C. K.; Iton, L. E.; Ozawa, M. Hydrogen Vibrational Density of States of Adsorbed Water on Rare-Earth Modified Zirconia. *Phys. B* **1995**, *213-214* (C), 640−642.
(52) Loong, C. K.; Richardson, J. W.; Ozawa, M. Crystal Phases, Defects, and Dynamics of Adsorbed Hydroxyl Groups and Water in Pure and Lanthanide-Modified Zirconia: A Neutron-Scattering Study. *J. Catal.* **1995**, *157* (2), 636−644.
(53) Peet, J. R.; Fuller, C. A.; Frick, B.; Koza, M.; Johnson, M. R.; Piovano, A.; Evans, I. R. Insight into Design of Improved Oxide Ion Conductors: Dynamics and Conduction Mechanisms in the $Bi_{0.913}V_{0.087}O_{1.587}$ Solid Electrolyte. *J. Am. Chem. Soc.* **2019**, *141* (25), 9989−9997.
(54) Peet, J. R.; Fuller, C.; Frick, B.; Zbiri, M.; Piovano, A.; Johnson, M. R.; Evans, I. R. Direct Observation of Oxide Ion Dynamics in $La_2Mo_2O_9$ on the Nanosecond Timescale. *Chem. Mater.* **2017**, *29*, 3020−3028.
(55) Waroquiers, D.; Gonze, X.; Rignanese, G. M.; Welker-Nieuwoudt, C.; Rosowski, F.; Göbel, M.; Schenk, S.; Degelmann, P.; André, R.; Glaum, R.; et al. Statistical Analysis of Coordination Environments in Oxides. *Chem. Mater.* **2017**, *29* (19), 8346−8360.
(56) Abakumov, A. M.; Shpanchenko, R. V.; Lebedev, O. I.; Van Tendeloo, G.; Amelinckx, S.; Antipov, E. V. The Phase Transitions and Crystal Structures of $Ba_3RM_2O_{7.5}$ Complex Oxides (R = Rare-Earth Elements, M = Al, Ga). *Acta Crystallogr., Sect. A: Found. Crystallogr.* **1999**, *55* (5), 828−839.
(57) Wang, C. H.; Guo, D. F.; Li, Z. F.; Wang, X. M.; Lin, J. H.; Zeng, Z. Z.; Jing, X. P. Crystal Structure of $Sr_6Y_2Al_4O_{15}$: XRD

Refinements and First-Principle Calculations. *J. Solid State Chem.* **2012**, *192*, 195−200.
(58) Luo, K.; Hayward, M. A. Complex Cation Order in Anion-Deficient $Ba_nYFe_{n-1}O_{2.5n}$ Perovskite Phases. *Inorg. Chem.* **2012**, *51* (22), 12281−12287.
(59) Luo, K.; Tran, T. T.; Halasyamani, P. S.; Hayward, M. A. Synthesis and Selective Topochemical Fluorination of the Cation and Anion-Vacancy Ordered Phases Ba_2YCoO_5 and $Ba_3YCo_2O_{7.5}$. *Inorg. Chem.* **2013**, *52* (23), 13762−13769.
(60) Arroyabe, E.; Kaindl, R.; Többens, D. M.; Kahlenberg, V. $K_2Ca_6Si_4O_{15}$-Structural and Spectroscopical Studies on a Mixed Tetrahedral-Octahedral Framework. *J. Solid State Chem.* **2009**, *182* (12), 3254−3261.
(61) Ben Yahia, H.; Gaudin, E.; Boulahya, K.; Darriet, J. Synthesis, Structure and Magnetic Properties of the New Oxygen-Deficient Perovskite $Na_3MnV_2O_{7.5}$. *Solid State Sci.* **2011**, *13* (6), 1235−1241.
(62) King, G.; Thompson, C. M.; Luo, K.; Greedan, J. E.; Hayward, M. A. Identifying the Local Structural Units in $La_{0.5}Ba_{0.5}MnO_{2.5}$ and $BaY_{0.25}Fe_{0.75}O_{2.5}$ through the Neutron Pair Distribution Function. *Dalt. Trans.* **2017**, *46*, 1145.
(63) Groom, C. R.; Bruno, I. J.; Lightfoot, M. P.; Ward, S. C. The Cambridge Structural Database. *Acta Crystallogr., Sect. B: Struct. Sci., Cryst. Eng. Mater.* **2016**, *72* (2), 171−179.

https://dx.doi.org/10.1021/acs.chemmater.0c01378
Chem. Mater. 2020, 32, 4347−4357